Supporting Information for
High-Resolution Direct Laser Writing Nanolithography Enabled by Oxidation-Mediated Corrosion Selectivity in N-Doped Sb Heat-Mode Resists

Jialong Guo#, Lihao Sun#, Ying Wang, Tao Wei*, Bo Liu**

Suzhou Key Laboratory for Nanophotonic and Nanoelectronic Materials and Its Devices, School of Materials Science and Engineering, Suzhou University of Science and Technology, Suzhou 215009, Jiangsu Province, China

#The authors contribute equally to this work.

* Corresponding author: E-mail address: weitao@usts.edu.cn

** Corresponding author: E-mail address: liubo@mail.usts.edu.cn

S1 Chemical Compositions of NSb Thin Films

Table S1 Atomic concentrations of N doped Sb thin films.

N_2/Ar flow ratio (SCCM)	2:50	4:50	6:50	8:50	10:50	12:50	14:50
N (at.%)	1.6	3.1	5.3	6.0	7.2	10.9	11.5
Sb (at.%)	98.4	96.9	94.7	94.0	92.8	89.1	88.5

S2 Dependence of Resistance on Temperature in NSb Thin Films

In **Figure S1**(a), at each N concentration, the resistance of the NSb thin film gradually decreases with the increase in temperature owing to its semiconductor characteristics. However, the resistance sharply decreases when the temperature is higher than a critical point, which is defined as the crystallization temperature (T_c), indicating the occurrence of the phase-change process. To accurately determine the T_c of the NSb thin film, **Figure S1**(b) shows the derivative of resistance with respect to temperature (dR/dT) curves at various N concentrations. T_c is defined as the peak valley in the dR/dT curves and further marked in the figure. With the increase in N concentration, the T_c gradually increases from 142 °C to 236 °C, revealing the enhanced thermal stability of NSb films after N doping.

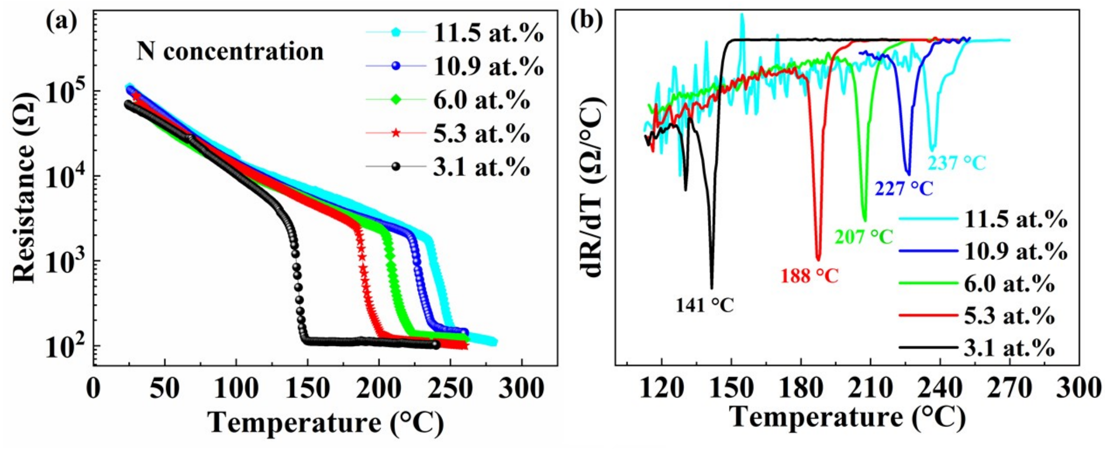

Figure S1(a) Dependence of resistance on temperature in NSb thin films with various N concentrations; (b) the derivative of resistance to temperature (dR/dT) curves at various N concentration.

S2 Developing Selectivity and Corresponding Chemical Reactions

The corrosion reaction can be expressed as follows: Firstly, laser exposure results in the oxidization of NSb thin film and the formations of Sb_2O_3/Sb_2O_5 and NO/NO_2 as follows.

$$4Sb + 3O_2 \rightarrow 2Sb_2O_3 \quad (1)$$

$$4Sb + 5O_2 \rightarrow 2Sb_2O_5 \quad (2)$$

$$2N + O_2 \rightarrow 2NO\uparrow \quad (3)$$

$$N + O_2 \rightarrow NO_2\uparrow \quad (4)$$

The formed Sb oxides are further dissolved into TMAH solution by following reactions.

$$Sb_2O_3 + 2OH^- \rightarrow 2SbO_2^- + H_2O \quad (5)$$

$$Sb_2O_5 + 2OH^- \rightarrow 2SbO_3^- + H_2O \quad (6)$$

Because the NSb thin film in the exposed state has a higher oxidation degree than in the as-deposited state, it is more susceptible to corrosion by the TMAH solution. In contrast, the as-deposited film features uniformly dispersed N and Sb atoms, which helps restrain the oxidation and dissolution of Sb atoms to some extent. Consequently, the corrosion rate of the exposed film surpasses that of the as-deposited film, resulting in corrosion selectivity.

Table S2 Binding energies of Sb 4d and N1s core-levels in NSb thin films at different conditions.

Sample	Binding energy (eV)						
	Sb 4d				N 1s		
Peak	A	B	C	D	A	B	C
As-deposited film-Ar$^+$ etching	-	-	33.2	31.9	403.6	-	396.5
As-deposited film	35.5	34.3	33.2	31.9	401.3	399.7	396.5
As-deposited film-TMAH	35.5	34.2	33.1	31.9	402.3	399.7	396.5
Exposed film- Ar$^+$ etching	-	-	33.3	32.0	403.8	-	396.6
Exposed film	35.6	34.4	33.3	32.1	401.5	399.9	396.6
Exposed film-TMAH	35.3	34.1	33.0	31.8	402.5	399.6	396.3

S3 X-ray Reflectivity Curves of As-deposited and Crystalline NSb Thin Films

X-ray reflectivity (XRR) data are measured and GenX software[1-3] is further adopted to fit the XRR data to obtain the thickness, mass density and roughness of as-deposited and crystalline NSb thin films, as shown in **Figure S2**. One can see the good agreement between measured and fitting curves for both amorphous and crystalline films (**Figure S2**(a)), suggesting the reliable fitting results. In **Figure S2**(b), the fitted mass density and roughness both increase while thickness reduces from amorphous to crystalline state.

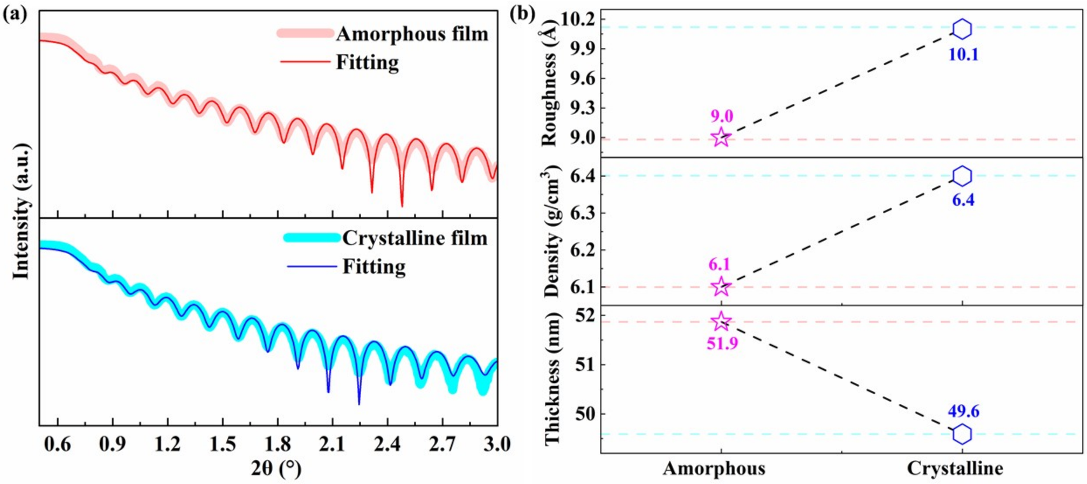

Figure S2(a) XRR curves, and (b) interfacial roughness, mass density, and thickness evolution from amorphous to crystalline film.

S4 Optical Constants of NSb Thin Films

The wavelength-dependent refractive index (n) and extinction coefficient (k) of as-deposited and crystalline NSb thin films are shown in **Figure S3**, which are fitted by Tauc-Lorentz and Lorentz oscillator models based on ellipsometry. The fitting parameters are listed in **Table S3**, all presenting good agreement between experimental and fitting data with low root mean square error (MSE). One can see the obvious difference in optical constants between as-deposited and crystalline films. For example, at 405 nm wavelength, the n and k of the as-deposited film are 2.29 and 3.05, respectively. In the crystalline film, the n and k at 405 nm wavelength are 1.36 and 3.48, respectively.

Table S3 Fitting parameters of as-deposited and crystalline NSb thin films via Tauc-Lorentz and Lorentz oscillator model.

Material	Fitting model parameters								Thickness (nm)	MSE
	Oscillator Model	Tauc-Lorentz				Lorentz				
	Parameter	A	C	E_n	E_g	A	E_n	B_r		
As-deposited NSb	Value	64.2	2.4	3.2	0	12.0	1.0	0.7	48.0	9.3
Crystalline NSb		23.4	1.8	1.6	0	54.7	0.9	2.1	45.7	10.5

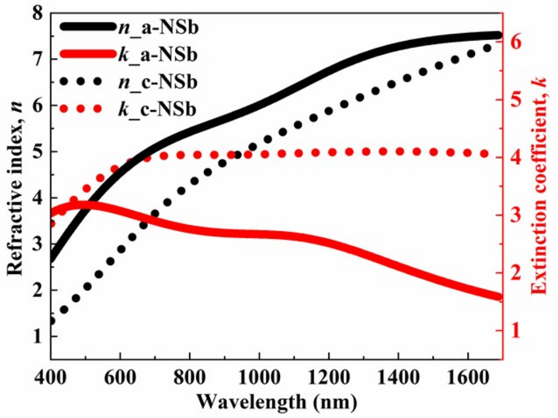

Figure S3 Optical constants (*n, k*) of deposited (a-NSb) and crystalline NSb (c-NSb) films.

S5 Molecular Dynamics Simulation and Thermal Conductivity Calculation

To determine the thermal conductivity of N doped Sb thin film, a molecular dynamics (MD) model was constructed using LAMMPS (Large-scale Atomic/ Molecular Massively Parallel Simulator) platform[4, 5]. The simulation workflow comprises the following key steps:

Initialization and Lattice Construction: The simulation employed the metal unit system (with units of energy: eV, length: Å, time: ps) and constructed a face-centered cubic (FCC) Sb lattice with a lattice constant of 4.506 Å. The simulation cell dimensions were set to 30×30×80 unit cells to ensure computational accuracy. The cross-sectional area (30×30 cells) was chosen to be sufficiently large to mitigate finite-size effects[6]. This configuration minimizes spurious phonon scattering caused by confined transverse dimensions, thereby improving the reliability of thermal conductivity predictions.

Atomic Substitution and Potential Setup: In pure Sb system, Sb atoms with 3.1 at.% concentration were replaced by N atoms to form an N-Sb system. Interatomic interactions were modeled using the Lennard-Jones (L-J) potential with energy (ε) and atomic diameter (σ) calibrated as follows: Sb-Sb ($\varepsilon \approx 0.01947$ eV, $\sigma \approx 4.42$ Å), N-N ($\varepsilon \approx 0.00299$ eV, $\sigma \approx 3.66$ Å) and Sb-N ($\varepsilon \approx 0.00764$ eV, $\sigma \approx 4.04$ Å)[7].

Energy Minimization and Annealing: Structural optimization was performed with convergence criteria of 1×10^{-5} eV/Å (force) and 1×10^{-7} eV (energy). Subsequently, the system was equilibrated under the NVT (constant number of atoms, volume and temperature) ensemble at 800 K for 50,000 steps to eliminate residual stresses.

Thermal Transport Simulation: A temperature gradient was established by continuously applying a heat flux to the hot region while extracting an equivalent amount of heat flux from the cold region, thereby imposing a net heat flux across the system. A heat flux of $Q = 0.05$ eV/ps was selected to achieve a measurable temperature gradient while avoiding nonlinear effects, ensuring a satisfactory signal-to-noise ratio[6]. Temperature profiles along the z-direction were recorded every 5000 steps during a production phase of 5000000 steps to verify steady-state conditions, as shown in **Figure S4**.

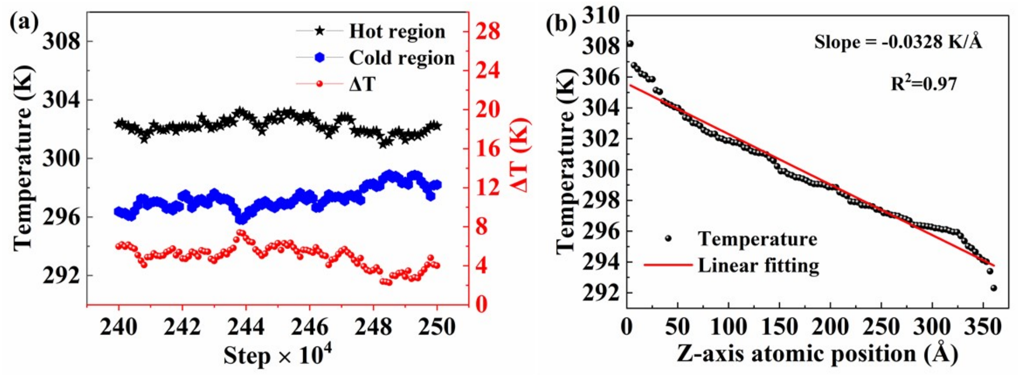

Figure S4(a) After the steady state is reached, the temperature distribution of the cold and hot regions and their temperature differences (ΔT); (b) the temperature of atoms at different positions along the Z axis after reaching a steady state.

In **Figure S4**(a), the hot region stabilizes at 302.2 K while the cold region equilibrates at 297.3 K, maintaining a temperature difference (ΔT) of 4.9 K with fluctuations of approximately ±1 K during the equilibrium state. **Figure S4**(b) displays the steady-state temperature profile along the z-direction. A linear fit of the temperature profile yields a slope of -0.0328 K/Å with a goodness-of-fit value of R^2=0.97, confirming consistency with Fourier's law. Thermal conductivity (κ) is subsequently calculated using Fourier's law[6],

$$\kappa = -\frac{Q \cdot L}{A \cdot \Delta T} \tag{I}$$

where Q (= 0.05 eV/ps) is the heat flux, L (= 360.48 Å) is the heat transfer length, and A (= 18273.63 $Å^2$) is the cross-sectional area. The temperature gradient is given by $\Delta T/L$ (= -0.0328 K/Å). Therefore, the thermal conductivity κ of the NSb thin film is calculated to be 0.1335 W/(m·K).

S6 Heat Capacity Calculation of NSb Thin Films via Dulong-Petit Law

The isobaric heat capacity (C_p) of NSb thin film with a N concentration of 3.1 at.% was calculated using Dulong-Petit law[8, 9]. The detailed procedure is outlined below:

Atomic Percentage to Molar Fraction: In 1 molar NSb thin film, N atom occupies 0.031 molar (*that is*, n_N=0.031 mol) while Sb atom occupies 0.969 molar (*that is*, n_{Sb}=0.969 mol).

Total Molar Heat Capacity: According to the Dulong-Petit law, each atom contributes 3R to the molar heat capacity, where R is the gas constant (R=8.314

J/mol/K). Therefore, the total molar heat capacity ($C_{p,\,molar}$) of a 1-molar NSb thin film is 24.94 J/K, calculated using the following formula:

$$C_{p,molar} = (n_N + n_{Sb}) \times 3R \tag{II}$$

Total Mass Calculation: For a 1 molar NSb thin film, the molar masses of N (M_N) and Sb (M_{Sb}) atoms are 14.01 g/mol and 121.76 g/mol, respectively. Using the following formulas, the corresponding masses of N (m_N) and Sb (m_{Sb}) are calculated as 0.43 g and 117.99 g, respectively.

$$m_N = n_N \times M_N \tag{III}$$

$$m_{Sb} = n_{Sb} \times M_{Sb} \tag{IV}$$

Therefore, the total mass of a 1-molar NSb thin film is 118.42 g, calculated using the following formula.

$$m_{total} = m_N + m_{Sb} \tag{V}$$

Specific Heat Capacity Conversion: The specific heat capacity (C_p) is obtained by dividing the total molar heat capacity by the mass per mole, resulting in a value of 210.61 J/(kg·K) according to the following formula.

$$C_p = \frac{C_{p,molar}}{m_{total}} \tag{VI}$$

S7 Details of Thermal Field Simulation

A three-dimensional transient opto-thermal simulation model was developed using COMSOL software, building upon prior research[10]. A three-layer geometric model is established, consisting of a 50 nm-thick air layer, a 100 nm-thick NSb thin film, and a 100 nm-thick Si substrate. The simulation domain is set to 1.8 μm × 1.8 μm. The laser wavelength (λ) is 405 nm and pulse width (R_{ect}) is 10 ns as well as the focused spot radius (w_0) of 0.3 μm. The NSb film is treated as an isotropic material with uniform thermal properties. Relevant material parameters are listed in **Table 2** of the main text.

The time-dependent transient heat transfer process is governed by equation (VII).

$$\rho C_p \frac{\partial T}{\partial t} = k\nabla^2 T + Q_h(r,z) \tag{VII}$$

where ρ is the mass density, C_p is the heat capacity, k is the thermal conductivity, and T is the temperature. Considering the heat exchange between the NSb film and the surrounding environment along both radial (r) and thickness (z) directions, a convective boundary condition is applied by equation (VIII).

$$-k\frac{\partial T}{\partial n}=h(T-T_0) \tag{VIII}$$

where h and T_0 are heat exchange coefficient (h = 1200 W/m^2/K) and ambient temperature (T_0 = 293.15 K), respectively. n is the normal direction of the boundary, including r and z directions. $Q_h(r, z)$ is the laser-induced heat quantity in the thin films along the r and z directions, expressed by equations (IX).

$$Q_{heat}(r,z)=\alpha\times I(r,z)\times R_{ect} \tag{IX}$$

where α is absorption coefficient, defined as $4\pi k/\lambda$ and k is extinction coefficient. R_{ect} denotes the width of laser pulse. I(r, z) is the laser intensity along the r and z directions, expressed by equation (X).

$$I(r,z)=\frac{2P}{\pi w^2(z)}exp[-\frac{2r^2}{w^2(z)}] \tag{X}$$

$w(z)$ is waist radius of laser beam along the z direction, further obtained by equation (XI).

$$w(z)=w_0\sqrt{1+{}^{z}/{z_0}^2} \tag{XI}$$

z_0 is the Rayleigh length, determined by equation (XII).

$$z_0=\pi w_0^2/\lambda \tag{XII}$$

According to equations (VII)-(XII), thermal distribution of NSb thin film can be obtained.

S8 Pattern Transfer and Sidewall Profile Control in Silicon

Figure S5 and **Figure S6** present the etching morphologies of Si patterns transferred from NSb thin films under different chamber pressures and SF_6/O_2 flow ratios, respectively. As shown in **Figure S5** and **Figure 5**(d, e), as the chamber pressure increases, the etching linewidth, depth, and line edge roughness (LER) all progressively increase, while the sidewall steepness deteriorates. It is noted that the linewidth and period of NSb mask both are fixed before Si etching. This can be attributed to the increased concentration of F radicals at a fixed $SF_6/(SF_6+O_2)$ flow ratio (0.83) and etching power (100 W), which intensifies the chemical etching effect. Additionally, higher chamber pressure enhances interparticle collisions, disrupting the directional motion of particles and consequently reducing sidewall steepness. At a pressure as low as 10 mTorr, steep sidewalls with low LER are achieved, along with the linewidth of 553 nm and period of 1 μm.

For the fine structures with narrower linewidths, the $SF_6/(SF_6+O_2)$ flow ratio is further optimized at a fixed pressure of 10 mTorr and an etching power of 100 W. Prior to silicon etching, the linewidth and period of the NSb mask remain unchanged. As illustrated in **Figure S6** and **Figure 5**(f, g), with increasing $SF_6/(SF_6+O_2)$ flow ratio, the etched linewidth gradually increases, while the LER shows minimal variation. Moreover, the sidewall steepness initially improves but then deteriorates. At an $SF_6/(SF_6+O_2)$ flow ratio of 0.75, optimal sidewall steepness is achieved, accompanied by a linewidth of 305 nm and period of 600 nm. This specific flow ratio likely provides an ideal balance between the chemical etching species (F radicals) and the passivation agents (O radicals), which protect the sidewalls from corrosion and thereby enhance anisotropic etching.

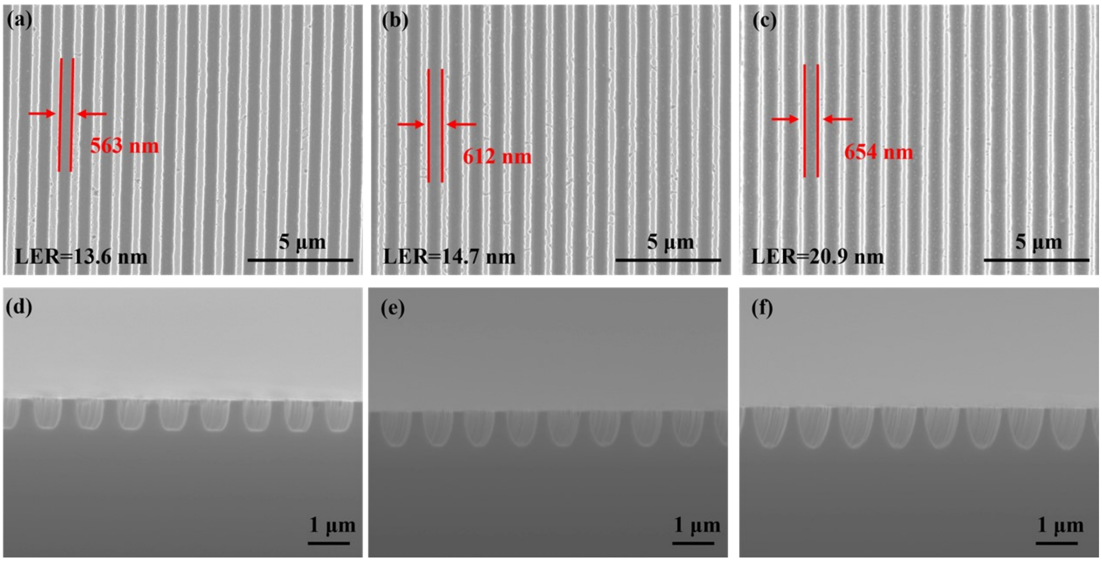

Figure S5 Influence of chamber pressure on the etching profile of silicon gratings: (a-d) Top-view and (e-h) corresponding cross-sectional SEM images etched at the pressures of (a, e) 30 mTorr, (b, f) 50 mTorr, (c, g) 70 mTorr, respectively.

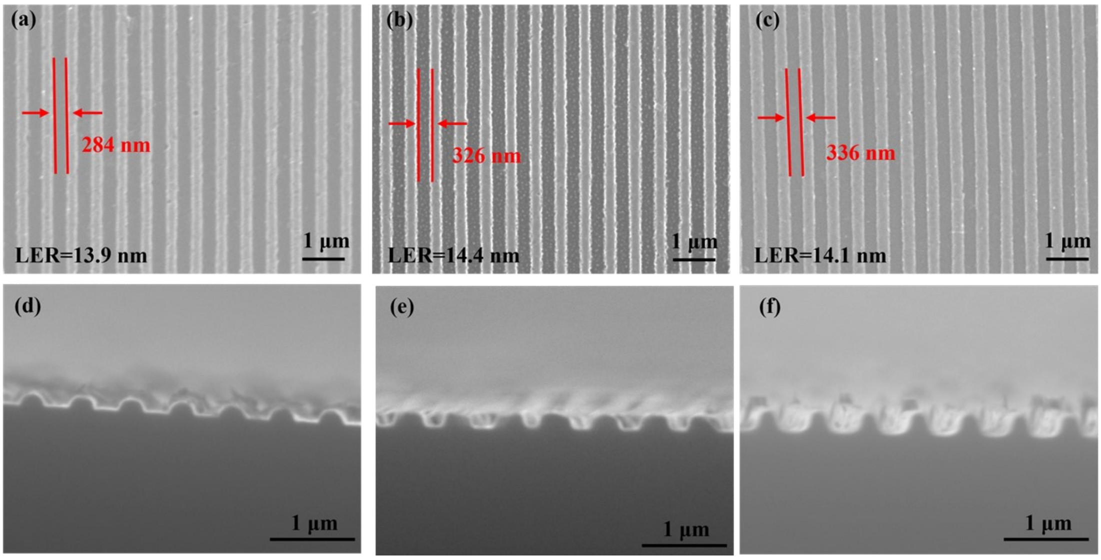

Figure S6 Influence of SF_6/O_2 flow ratio on the etching profile of silicon gratings: (a-d) Top-view and (e-h) corresponding cross-sectional SEM images etched at the $SF_6/(SF_6+O_2)$ flow ratios of (a, e) 0.67, (b, f) 0.80, and (c, g) 0.83, respectively.

S9 Dry Etching Mechanism and Corresponding Chemical Reactions

The etching selectivity mechanism is elucidated as follows: Under the bombardment of high-energy electrons, SF_6 molecules undergo dissociation, producing fluoride radicals (F*) and SF_x^+ products as follows.

$$SF_6 + e^- \rightarrow (6-x)F^* + SF_x^+ + e^- \quad (x=1\sim5) \tag{7}$$

O_2 molecules dissociate into oxygen radicals (O*) in the SF_6/O_2 plasma.

$$O_2 + e^- \rightarrow 2O^* + e^- \tag{8}$$

In parallel, SF_6 can react with O_2 in the chamber to form sulfur oxyfluorides (SO_2F_2) and F*.

$$SF_6 + O_2 \rightarrow 4F^* + SO_2F_2 \tag{9}$$

The dissociated O* can react with Si to form SiO_2 component.

$$Si + 2O^* \rightarrow SiO_2 \tag{10}$$

Si and the formed SiO_2 both can react with F* to produce the volatile SiF_4 product through the following reactions.

$$Si + 4F^* \rightarrow SiF_4\uparrow \quad (11)$$

$$SiO_2 + 4F^* \rightarrow SiF_4\uparrow + O_2 \quad (12)$$

The introduction of O_2 not only promotes the generation of F*, but also enhances the physical bombardment effect. Therefore, the Si substrate is readily etched under SF_6/O_2 plasma.

For the NSb thin film, the Sb element can react with O* to form non-volatile SbO_x (x=3/2 or 5/2) components as follows.

$$Sb + xO^* \rightarrow SbO_x\downarrow \quad (13)$$

Sb element and the formed SbO_x components can further react with F* to produce non-volatile SbF_x (x=3 or 5) components.

$$Sb + xF^* \rightarrow SbF_x\downarrow \quad (14)$$

In addition, the N element can react with O* to obtain NO_x component under the plasma.

$$N + xO^* \rightarrow NO_x \quad (15)$$

The formation of non-volatile SbO_x and SbF_x is beneficial for enhancing the etching resistance of the NSb thin film and reducing the etching rate. As a result, high etching selectivity between Si and the NSb thin film can be achieved.

Table S4 Binding energies of Sb 4d, Sb 3d and O 1s, N 1s, and F 1s core-levels derived from XPS spectra of SF_6/O_2-etched NSb thin film.

Element	**Binding energy (eV)**												
	Sb 4d				**Sb 3d & O 1s**					**N 1s**		**F 1s**	
Peak	A	B	C	D	A	B	C	D	E	A	B	A	B
Ar^+ etching 0 s	35.6	34.3	33.4	32.2	539.9	537.7	530.5	531.0	528.3	400.4	-	688.3	684.6
Ar^+ etching 18 s	35.4	34.1	33.0	31.8	539.5	537.2	530.2	530.1	527.9	-	396.7	-	684.1
Ar^+ etching 36 s	35.2	33.9	32.9	31.7	539.4	537.1	530.1	529.6	527.7	-	396.3	-	684.1

References

1. Guo, T.; Song, S.; Song, Z.; Ji, X.; Xue, Y.; Chen, L.; Cheng, Y.; Liu, B.; Wu, L.; Qi, M.; Feng, S., SiC-doped $Ge_2Sb_2Te_5$ phase-change material: a candidate for

high-density embedded memory application. *Advanced Electronic Materials* **2018,** *4* (8), 1800083.

2. Björck, M.; Andersson, G., GenX: an extensible X-ray reflectivity refinement program utilizing differential evolution. *Journal of Applied Crystallography* **2007,** *40* (6), 1174-1178.

3. Glavic, A.; Björck, M., GenX 3: the latest generation of an established tool. *Journal of Applied Crystallography* **2022,** *55* (4), 1063-1071.

4. Huang, Z.; Tang, Z.; Yu, J.; Bai, S., Thermal conductivity of amorphous and crystalline thin films by molecular dynamics simulation. *Physica B: Condensed Matter* **2009,** *404* (12), 1790-1793.

5. Thompson, A. P.; Aktulga, H. M.; Berger, R.; Bolintineanu, D. S.; Brown, W. M.; Crozier, P. S.; in 't Veld, P. J.; Kohlmeyer, A.; Moore, S. G.; Nguyen, T. D.; Shan, R.; Stevens, M. J.; Tranchida, J.; Trott, C.; Plimpton, S. J., LAMMPS - a flexible simulation tool for particle-based materials modeling at the atomic, meso, and continuum scales. *Computer Physics Communications* **2022,** *271*, 108171.

6. Ozsipahi, M.; Jean, S.; Beskok, A.; Wilson, A. A., Molecular dynamics simulation of thermal conductivity of GaN. *International Communications in Heat and Mass Transfer* **2025,** *163*, 108658.

7. Rappe, A. K.; Casewit, C. J.; Colwell, K. S.; Goddard, W. A., III; Skiff, W. M., UFF, a full periodic table force field for molecular mechanics and molecular dynamics simulations. *Journal of the American Chemical Society* **1992,** *114* (25), 10024-10035.

8. Agne, M. T.; Imasato, K.; Anand, S.; Lee, K.; Bux, S. K.; Zevalkink, A.; Rettie, A. J. E.; Chung, D. Y.; Kanatzidis, M. G.; Snyder, G. J., Heat capacity of Mg_3Sb_2, Mg_3Bi_2, and their alloys at high temperature. *Materials Today Physics* **2018,** *6*, 83-88.

9. Andritsos, E. I.; Zarkadoula, E.; Phillips, A. E.; Dove, M. T.; Walker, C. J.; Brazhkin, V. V.; Trachenko, K., The heat capacity of matter beyond the Dulong–Petit value. *Journal of Physics: Condensed Matter* **2013,** *25* (23), 235401.

10. Li Z, Wei T, Sun L*, et al.* High-resolution multilevel reversible color printing based on Sb_2S_3 phase change materials[J]. Photonics Research, 2025, **13**: 661-670.